

# The Seasonal and Interannual Variability of the Budgets of $\text{N}_2\text{O}$ and $\text{CCl}_3\text{F}$

Sun Wong<sup>1</sup>

Physics Department, Columbia University, New York.

Michael J. Prather<sup>2</sup>

Earth System Science, University of California at Irvine.

David H. Rind<sup>3</sup>

NASA Goddard Space Flight Center, Institute for Space Studies, New York.

---

<sup>1</sup>Now at Atmospheric Sciences Research Center, 251 Fuller Road, Albany, NY 12203.  
(email: wong@climate.cestm.albany.edu)

<sup>2</sup>Earth System Science Department, University of California, Irvine, CA 92717. (email: prather@halo.ps.uci.edu)

<sup>3</sup>Goddard Institute for Space Studies, 2880 Broadway, New York, NY 10025. (email: drind@giss.nasa.gov)

## Abstract

The 6-year wind archives from the Goddard Institute for Space Studies/Global Climate-Middle Atmosphere Model (GISS/GCMAM) were input to the GISS/Harvard/Irvine Chemical Transport Model (G/H/I CTM) to study the seasonal and interannual variability of the budgets and distributions of nitrous oxide ( $\text{N}_2\text{O}$ ) and trichlorofluoromethane ( $\text{CCl}_3\text{F}$ ), with the corresponding chemical loss frequencies recycled and boundary conditions kept unchanged from year to year. The effects of ozone feedback and quasi-biennial oscillation (QBO) were not included. However, the role of circulation variation in driving the lifetime variability is investigated. It was found that the global loss rates of these tracers are related to the extratropical planetary wave activity, which drives the tropical upward mass flux. For  $\text{N}_2\text{O}$ , a semiannual signal in the loss rate variation is associated with the interhemispheric asymmetry in the upper stratospheric wave activity. For  $\text{CCl}_3\text{F}$ , the semiannual signal is weaker, associated with the comparatively uniform wave episodes in the lower stratosphere. The loss rates lag behind the wave activity by about 1-2 months. The interannual variation of the GCM generated winds drives the interannual variation of the annually averaged lifetime. The year-to-year variations of the annually averaged lifetimes can be about 3% for  $\text{N}_2\text{O}$  and 4% for  $\text{CCl}_3\text{F}$ .

## 1 Introduction

The relationship between the stratospheric wave activity and the meridional distribution of long-lived tracers was discussed by Holton (1986). The isopleths of a long-lived tracer are balanced by the transport due to diabatic circulation, horizontal eddy transport, and chemical loss in the stratosphere. The diabatic circulation steepens the isopleths, but both the horizontal eddy transport and the chemical loss tend to flatten the isopleths. Since both the diabatic circulation and the horizontal eddy transport are controlled by wave activity [Holton, 1986; Holton et al., 1996], the effects of wave activity on the long-lived tracer

distributions are complicated. Greater wave activity can steepen the isopleths across subpolar latitudes by strengthening the diabatic circulation, but flatten the isopleths by enhancing the horizontal eddy transport. The effect of these opposing mechanisms was well illustrated by the different rates of descent of methane ( $\text{CH}_4$ ) and  $\text{N}_2\text{O}$  in the polar vortex [Strahan et al., 1996].

In the tropics, the upward mass flux across the tropopause is controlled by the extratropical wave activity [Haynes et al., 1991; Holton et al., 1996]. The annual mean of the mass flux across the tropical 100 mb surface is estimated to be  $85 \times 10^8$  kg/s with significant seasonal variation ( $114 \times 10^8$  kg/s in December-January-February (DJF) and  $56 \times 10^8$  kg/s in June-July-August (JJA)) [Rosenlof and Holton, 1993]. This seasonal variation of the tropical upward mass flux induces an observable annual cycle of lower stratospheric temperatures in the tropics [Yulaeva et al., 1994; Rosenlof, 1995 and references therein]. Interannual variation of the tropical upward mass flux was also derived from United Kingdom Meteorological Office (UKMO) assimilated temperatures and National Meteorology Center (NMC) temperatures [Rosenlof, 1995].

Both  $\text{N}_2\text{O}$  and  $\text{CCl}_3\text{F}$  are long-lived tracers with tropospheric sources, and not effectively removed in the troposphere. They are transported into the stratosphere through the tropical tropopause and dissociated in the stratosphere by chemical processes, providing constituents that trigger the catalytic destructions of stratospheric ozone. The  $\text{N}_2\text{O}$  lifetime derived from observations is about 120 yrs [Prather et al., 1994; Minschwaner et al., 1998] and  $124 \pm 49$  yrs [Volk et al., 1997], and that derived from previous 2-D models is in the range of 120-139 yrs [Ko and Jackman, 1994]. The  $\text{CCl}_3\text{F}$  lifetime derived from observations is 50 yrs [Prather et al., 1994], 34-47 yrs [Ko and Jackman, 1994],  $52^{+23}_{-12}$  yrs [Cunnold et al., 1997] and  $41 \pm 12$  yrs [Volk et al., 1997], and that derived from the 2-D models is 40-60 yrs [Ko and Jackman, 1994].

In this paper, the seasonal and interannual variability in the  $\text{N}_2\text{O}$  and  $\text{CCl}_3\text{F}$  lifetimes is examined with a 3-D model, which is required for investigation of the impacts of planetary wave on the tracers' budgets since parameterization for the eddy transport are not necessary in 3-D models. The interannual variation

in ozone transport and quasi-biennial oscillation (QBO) are not included. This paper is the first step to understand the role of the variation in wave activity in driving the lifetime variations, without any feedback from ozone response and modulation by QBO. In section 2, the models used are described. Section 3 discusses the simulation results. Discussion and conclusions are included in section 4.

## 2 The Models

The tracer experiments used the 21-layer Chemical Transport Model (CTM) [Prather, 1993], which advects chemical constituents with winds produced from the 23-layer GISS Global Climate/Middle Atmospheric Model (GISS/GCMAM) [Rind et al., 1988a and 1988b]. The GISS/GCMAM has been analyzed for a range of climate change experiments [Rind et al., 1990, 1992; Rind and Balachandran, 1995; Rind and Lonergan, 1995; Shindell et al., 1997], etc. The CTM adopts the  $7.83^\circ \times 10^\circ$  grid of the parent GCM for its horizontal resolution and uses vertical layers extending from the surface to 0.004 mb (about 85 km). The tropospheric layers, from 1 to 9, use sigma coordinates, while the stratospheric layers, from 10 to 21, use fixed pressure levels beginning above 100 mb. The top three layers of the 23-layer GCM are combined into the top layer of the CTM.

Boundary conditions for trace gas mixing ratios are applied in the lowest three layers (up to 1 km), which can be either fixed or varying in time. The chemistry of  $\text{N}_2\text{O}$  and  $\text{CCl}_3\text{F}$  is parameterized by their zonally and monthly averaged loss frequencies. These parameters are calculated from a photochemical box model using observed climatic values for temperature, ozone, and other trace gases [Avallone and Prather, 1997; Prather and Jaffe, 1990]. Parameterized convection and the associated horizontal diffusion occur in the troposphere, but not in the stratosphere. The advecting scheme conserves first- and second-order moments of the tracer distribution [Prather, 1986]. The CTM has been used to study tropospheric distribution of CFCs, dilution of the ozone hole, the

space shuttle impacts, seasonal evolutions of  $\text{N}_2\text{O}$ ,  $\text{O}_3$ , and  $\text{CO}_2$ , and tracer-tracer correlations [Avallone and Prather, 1997; Hall and Prather, 1993, 1995; Prather et al., 1987, 1990, 1993].

The GISS/GCMAM was used to produce 6-year wind archives and the associated diagnostics, especially E-P flux convergence which is a representative for planetary wave activity. The model provides generally realistic interannual variability in the mean circulations and planetary wave activity [Rind et al., 1988b]. The primary deficiencies of the model are somewhat reduced long-wave energy in the troposphere and lower stratosphere, too cold temperatures near the model top, and too warm temperatures in the Southern Hemisphere polar lower stratosphere.

Initial tracer distributions were calculated by recycling the first year of the GCM winds until a near steady-state repeating annual cycle was reached. The subsequent 5 years of winds are then put into the CTM sequentially. These runs are referred to as SEQUENTIAL runs. In order to compare our results with the steady state results, we ran another set of experiments in which each year's wind was recycled for about 10 years until a near steady-state was reached for that year's wind archive. These are referred to as STEADYSTATE runs (i.e., we have 6 individual near steady-state distributions for the corresponding 6-year wind archives). Since we initialized the tracers with the first year steady state distributions, all the first year results in the SEQUENTIAL runs match those in the STEADYSTATE runs. For all the experiments, the chemical loss frequencies and the tropospheric convection processes (not very important in these experiments) were recycled from year to year. The fixed chemical loss frequencies are equivalent to fixing the overhead column ozone amount; therefore, feedbacks from ozone response are not allowed in this study. The boundary condition of  $\text{N}_2\text{O}$  was fixed at 300 ppbv, and that of  $\text{CCl}_3\text{F}$ , at 250 pptv, for the lowest three levels of the CTM.

### 3 Results

#### 3.1 The Lifetimes

The lifetime of a chemical tracer is defined as the total mass (in kg) divided by the globally integrated loss rate (in kg/yr). Since the boundary conditions were fixed, the total mass of both tracers did not vary significantly over the years. Hence, the lifetimes are inversely proportional to the loss rates in our simulation results. The difference in global loss rates between the SEQUENTIAL and STEADYSTATE runs is small (about 3-4% from the mean values, see figs. 5 and 6) for our 6 years of meteorology. The differences in tracer distributions throughout the stratosphere are also small. Hereafter, our discussion will concentrate on the SEQUENTIAL runs.

Table 1 shows the seasonal and interannual variability of the lifetimes of both tracers in the SEQUENTIAL runs. The largest interannual difference in annual-mean lifetimes is about 3% for  $\text{N}_2\text{O}$  and about 4% for  $\text{CCl}_3\text{F}$  about their mean lifetimes. For both tracers, the seasonal variability is larger than the interannual variability. The interannual variability in the spring seasons (i.e. April (APR) or October (OCT)) is larger than that in the solstices (i.e. January (JAN) or July(JUL)). However, the interannual variability is reduced when the annual mean lifetime is taken. The model  $\text{N}_2\text{O}$  lifetime covers the range of 107-130 yrs, with the climatological mean of 121 yrs, consistent with those in Mahlman et al. (1986), Minschwaner et al. (1998), and Prather et al. (1994). The model  $\text{CCl}_3\text{F}$  lifetime covers the range of 30-34 yrs, with the climatological mean of 31.3 yrs, lower than those in Cunnold et al. (1997), Ko and Jackman et al. (1994), and Volk et al. (1997). This discrepancy in the  $\text{CCl}_3\text{F}$  lifetime may be due to the coarse vertical resolution (about 5 km in the stratosphere) applied by the CTM, which produces vertical mixing that is too rapid up to about 25 km [Avallone and Prather, 1997].

### 3.2 The Distributions

Since the  $\text{N}_2\text{O}$  loss is dominant in the upper stratosphere, the evolution of the zonal mean  $\text{N}_2\text{O}$  mixing ratio, averaged from 10 mb to 1 mb, is shown in figure 1a. In the tropics, there are primary peaks of mixing ratio, centered at about  $10^\circ\text{S}$ , during January to March, and secondary peaks of mixing ratio, centered at about  $10^\circ\text{N}$ , during June to September. These peaks of mixing ratio also correspond to the peaks of the loss rate shown in figure 5c. The location and time of the peaks agree with previous studies of the Cryogenic Limb Array Etalon Spectrometer (CLAES) data [Randel et al., 1994; Lou et al., 1997], in which primary peaks of  $\text{N}_2\text{O}$  mixing ratio were centered around  $10^\circ\text{S}$  during January to March in 1992 and 1993, while a secondary peak was centered around  $10^\circ\text{N}$  during August to October in 1992. However, it is hard to tell if the primary and secondary peaks had difference in magnitudes from these previous studies, although the model result of Lou et al. (1997) showed that the primary peaks had larger magnitude than the secondary peak at 10 mb. The annual cycle of the  $\text{N}_2\text{O}$  mixing ratio shown in figure 1a is also in general agreement with that of the  $\text{CH}_4$  mixing ratio shown in Randel et al. (1998, their fig. 9). The primary peak of  $\text{CH}_4$  mixing ratio at 2.2 mb was found during February to March, centered at about  $10^\circ\text{S}$ , and the secondary peak with about the same magnitude of the primary peak was found during August to September, centered at about  $10^\circ\text{N}$ . At 10 mb, the peak of  $\text{CH}_4$  mixing ratio reached maximum at the equator from November to June [Randel et al., 1998; fig. 9 in the reference]; therefore, one can expect the secondary peak is smaller in magnitude if the  $\text{CH}_4$  mixing ratio is averaged from 10 mb to 1 mb.

Figure 1b shows the evolution of the zonal mean  $\text{N}_2\text{O}$  flux across 10 mb. In the tropics, primary peaks of upward flux occur in December-January, whereas secondary peaks of upward flux occur in June, with magnitudes smaller than those of the primary peaks. The evolution of the mixing ratio is consistent with that of the flux, with a time lag of 1-2 months, that is from mid-winter, when the flux is maximum, to late winter and early spring, when the mixing

ratio is maximum. In high latitudes, peaks of upward flux can be seen around 70°N or 60°S, where polar descent (downward motion) should be expected. The zonal mean tracer flux includes the mean and eddy fluxes, and resembles the pattern of zonal mean circulation, instead of the Transformed Eulerian Mean (TEM or the residual) circulation, because the eddy flux is about 2-3 order of magnitude smaller. Therefore, the pattern of the zonal mean flux shown in figure 1b (as well as in fig. 2b for CCl<sub>3</sub>F) is consistent with the multi-cell structure of the zonal mean circulation, and the upward flux seen around 70°N or 60°S is an extension of the upward branch of the polar and the Ferrel cells from the troposphere. However, the polar upward flux occurring during polar nights less affects the lifetime and its variation because the loss is dominant in the tropics to the subtropics.

Similar results can be obtained for CCl<sub>3</sub>F if we consider a region in the lower stratosphere, because of the predominant CCl<sub>3</sub>F loss in this region. Figure 2a shows the zonal mean CCl<sub>3</sub>F mixing ratio, averaged from 100 mb to 10 mb, and figure 2b, the CCl<sub>3</sub>F upward flux across 100 mb. The seasonal evolution of subtropical to mid-latitude CCl<sub>3</sub>F mixing ratios (see the contour lines of 105-150 pptv in fig.2a) agree with that of the CH<sub>4</sub> mixing ratio at 68 mb in Randel et al. (1998), who found that the contour lines shift northward during July and southward during December to January as in our case of CCl<sub>3</sub>F mixing ratios. However, the CCl<sub>3</sub>F mixing ratio in the tropics shows less variability than those of N<sub>2</sub>O and CH<sub>4</sub> at the same levels. This may be due to the fact that CCl<sub>3</sub>F has larger photochemical loss in the tropics and behaves less as a passive tracer in this region. The seasonal variability of CCl<sub>3</sub>F mixing ratio recovers in higher latitudes where the photochemical loss is smaller.

### 3.3 Planetary Wave Activity and Upward Tracer Fluxes

The extratropical "suction pump" is believed responsible for driving the tropical upward mass flux which brings in tracers from the troposphere [Haynes et al., 1991; Holton et al., 1996]. The theory suggests that the tropical upward mass

flux is related to the extratropical wave activity, including both planetary and subgrid scale waves. Here we will consider only the impacts of planetary wave activity. Figure 3 shows the model evolution of planetary wave activity, represented by the E-P flux convergence averaged from 10 mb to 1 mb in figure 3a, and from 100 mb to 5 mb in figure 3b. In order to justify that the GISS/GCMAM has proper variability in planetary wave activity, the E-P flux divergence derived from NMC data from 1981-1995 is shown in figure 4 [Randel, 1992] (note that fig. 4 plots the E-P flux divergence so the shaded negative regions should be compared with the red positive regions in fig. 3). In the upper stratosphere (10-1 mb, fig. 3a and top panel of fig. 4), the model E-P flux convergence in middle latitudes reaches 2-3 m/s/day in northern hemisphere, and 1-2 m/s/day (2-3 m/s/day in the 4-th year) in southern hemisphere. This is consistent with the NMC E-P flux data, about 2.5 m/s/day in most of the years (5 m/s/day in some of the years) in northern hemisphere, and about 0-2.5 m/s/day (over 2.5 m/s/day in some of the years) in southern hemisphere. In the northern polar region, maxima over 5 m/s/day are seen in some of the years in both the model and NMC data. In the lower stratosphere (100-5 mb, fig. 3b and bottom panel of fig. 4), the model E-P flux convergence generally agrees with the NMC E-P flux convergence (2-3 m/s/day in northern hemisphere and 1-2 m/s/day in southern hemisphere). In both upper and lower stratosphere, the model can provide reasonable variability in planetary wave activity.

In the upper stratosphere (fig. 3a), strong wave episodes occur during autumn to early spring, from  $8^\circ$  to  $40^\circ$  in latitude, and drive larger tropical upward tracer flux. The interhemispheric asymmetry in the winter wave activity is associated with the seasonal asymmetry in the tropical upward flux, as well as the seasonal asymmetry in the  $\text{N}_2\text{O}$  loss. In the lower stratosphere (fig. 3b), wave episodes cover a range in time and latitude (from  $8^\circ$  to  $72^\circ$ ) that is wider than those in the upper stratosphere. The interhemispheric asymmetry in wave activity is less evident in the lower stratosphere. The distinction between primary and secondary peaks of the tropical  $\text{CCl}_3\text{F}$  flux and mixing ratio is also less evident.

The E-P flux convergence shown in Figure 3 is consistent with the tracer flux patterns shown in Figures 1b and 2b. In the upper stratosphere, peaks of downward tracer flux across 10 mb (fig. 1b) occur when the tropical upward tracer flux is at its maxima. This is because the E-P flux convergence from  $20^\circ$  to  $40^\circ$  (fig. 3a) provides poleward transport while the E-P flux divergence from  $50^\circ$  to  $70^\circ$  provides equatorward transport. The resultant horizontal tracer flux convergence produces downward tracer flux from  $40^\circ$  to  $50^\circ$  due to mass continuity. The downward tracer flux continues to lower altitude as shown in Figure 2b. In the 100 mb level (fig. 2b), the upward tracer flux appearing in the southern polar region is stronger than that in the northern polar region and may shift the spring time total ozone maxima toward lower latitudes in the southern hemisphere. This is consistent with the previous observational and model evolution of the total ozone, in which maxima of total ozone are seen during southern spring in the southern subpolar region (about 400 DU around  $50$ - $60^\circ$ S in September to October), whereas the maxima of total ozone during northern spring occur within the northern polar region (about 440 DU around  $80$ - $90^\circ$ N in March to April) [Bowman and Krueger, 1985; Ushimaru and Tanaka, 1994].

### 3.4 The Time Series

Time series of several averaged variables, representing different physical processes, are shown in figures 5 and 6 for  $\text{N}_2\text{O}$  and  $\text{CCl}_3\text{F}$ , respectively. Different tracers have different regions of dominant loss, and so only data in appropriate regions are used to produce the corresponding time series. Figure 5a is the averaged E-P flux convergence from  $8^\circ$  to  $40^\circ$  in latitude and from 10 mb to 1 mb in altitude, a region where the planetary wave activity is responsible for the tropical upward flux across 10 mb. The dotted and dashed lines represent the northern and southern wave activity, respectively. The tropical upward flux is driven by the combination of wave activity in both hemispheres; therefore, the sum is also plotted as the solid line. The spikes occurring during November

to March are mainly from the northern wave episodes, whereas those occurring during May to October are mainly from the southern wave episodes. Figure 5b is the  $\text{N}_2\text{O}$  flux averaged from  $24^\circ\text{S}$  to  $24^\circ\text{N}$ , a latitude range in which the  $\text{N}_2\text{O}$  flux is upward in the tropics, at 10 mb (fig. 1b). The time series of the flux is correlated with that of the wave activity.

Figures 5c and d show the variations of the global  $\text{N}_2\text{O}$  loss rate and mixing ratio, respectively. The mixing ratio is averaged from  $30^\circ\text{S}$  to  $30^\circ\text{N}$  in latitude and from 10 mb to 1 mb in altitude, a region in which the averaged  $\text{N}_2\text{O}$  mixing ratio reflects the tropical concentration variation (see fig. 1a). The solid lines are from the STEADYSTATE runs and the dotted lines are from the SEQUENTIAL runs. Primary peaks of mixing ratio occur during January to March, whereas secondary peaks occur during August to October, with magnitudes smaller than those of the primary peaks. This semiannual signal in the loss rate and the mixing ratio resembles the semiannual signal in the tropical upward flux across 10 mb (fig. 5b), which is driven by the asymmetric wave forcing from both hemispheres (fig. 5a). This result is consistent with Rosenlof (1995) in which a semiannual signal in the tropical upward mass flux above 10 mb was detected (fig. 15 in the reference).

The  $\text{CCl}_3\text{F}$  loss is dominant in the lower stratosphere, over a range of latitude wider than that found for the  $\text{N}_2\text{O}$  loss. Figure 6a is the averaged E-P flux convergence from  $8^\circ$  to  $72^\circ$  in latitude and from 100 mb to 5 mb in altitude, a region in which the averaged E-P flux convergence represents about 80% of the forcing of the tropical upward mass flux [Rosenlof, 1995]. The symbols in figure 6a are similar to those in figure 5a. Peaks of wave episodes are comparatively uniform in time. However, primary peaks during January to April are still evident. Figure 6b shows the time series of the upward  $\text{CCl}_3\text{F}$  flux across the tropical tropopause, represented by the flux averaged from  $30^\circ\text{S}$  to  $30^\circ\text{N}$  at 100 mb, a region where the tropical flux is mainly upward. The annual cycle is evident with peaks occurring during January to March. The time series of the  $\text{CCl}_3\text{F}$  loss rate and mixing ratio are shown in Figure 6c and d, respectively. The mixing ratio is averaged from  $50^\circ\text{S}$  to  $50^\circ\text{N}$  in latitude and from 100 mb

to 10 mb in altitude, a region with wider latitude range because the dominant loss of  $\text{CCl}_3\text{F}$  covers a wider range in latitude. The semiannual signal is less evident than that in the  $\text{N}_2\text{O}$  plots in figure 5, associated with the comparatively uniform wave episodes in the lower stratosphere. This is consistent with Rosenlof (1995), who found that the semiannual signal has a larger amplitude above 10 mb.

An estimate of the air mass flux across 100 mb can be obtained if the tracer fluxes and the corresponding tracer mixing ratios right below 100 mb are known. Table 2 shows the estimate of the tropical upward air mass flux across 100 mb from the CTM as well as the estimates from the previous literature. Our air mass flux is smaller than the estimate by Rosenlof and Holton (1993) during northern winter. However, during southern winter, our air mass flux is quite consistent with Rosenlof and Holton (1993). This is reasonable because GISS/GCMAM simulates weaker long-wave activity and the coarse resolution cannot resolve smaller-scale processes which may govern the troposphere-stratosphere exchange [Rind et al., 1988a]. Also shown in table 2 is the estimate by Rosenlof (1995) at 70 mb using the UKMO assimilated temperatures. Our CTM is consistent with Rosenlof (1995), recalling that our data were sampled at a lower altitude (100 mb) and thus should give slightly larger values than those at 70 mb. For the interannual variability in the tropical upward tracer fluxes (fig.5b and 6b), our CTM also gives reasonable variability which is similar to that shown in Rosenlof (1995) (their figure 11 shows a 2-year time series of the tropical upward mass flux at 70 mb).

### 3.5 The Time-Lag

From the correlations of the time series shown in figures 5 and 6, one can obtain the time lag between different physical processes. Figure 7 shows these cross correlations between the adjacent time series, which are obtained from the following formula:

$$corr(x, y, m) = \frac{\sum_i (x_i - \bar{x})(y_{i+m} - \bar{y})}{\sqrt{\sum_i (x_i - \bar{x})^2 \sum_i (y_i - \bar{y})^2}} \quad (1)$$

where  $m$  is the time lag from -12 to 12 months, overbar variables represent the mean (the average of 72 monthly data except for wave activity). For the wave activity, the mean is chosen to be the offset, which is zero in figure 5a but 1.0 in figure 6a, because the wave activity appears as spikes instead of a Gaussian distribution around the mean. This choice of the means for wave activity increases the correlation but does not change the time-lag between different processes. Since there are clear annual cycles in the time series, peaks of correlation around  $\pm 12$  months and anticorrelation around  $\pm 6$  months are expected. For  $N_2O$  (fig. 7a), the tropical upward flux at 10 mb lags the upper stratospheric wave activity by 1 month (dotted line); the loss lags the tropical upward flux by less than 1 month (dashed line); and the tropical upper stratospheric mixing ratio lags the loss by about 1 month (dash-dot line). The direct result is that the mixing ratio lags the wave activity by about 2 months (solid line). This result is consistent with Randel et al. (1998) who found a time-lag about 1 month between the  $CH_4$  maxima at 2.2 mb and the tropical upward motion at the same level. Since the horizontal eddy transport counteracts the transport caused by the mean vertical wind in the tropics, the years of the maximum wave activity and the maximum tropical upward flux does not coincide for  $N_2O$  (the second year for the wave activity but the third year for the tropical upward flux).

The story is different for  $CCl_3F$  (fig. 7b) because its predominant loss is in the lower-middle stratosphere. The correlation between the tropical upward flux and the lower stratospheric wave activity is small (about 0.3) and covers a broader time range (dotted line), which is associated with the comparatively uniform wave episodes in the lower stratosphere. The loss responds quite instantaneously to the tropical upward flux (time lag is less than 1 month, dashed line); and the lower stratospheric mixing ratio lags the loss by less than 1 month (dash-dot line). The direct correlation between the mixing ratio and the wave activity is, as expected, widespread, and it peaks at about 1 month time lag.

In our work, only planetary wave activity has been considered for the correlation calculations. GISS/GCMAM has parameterized gravity wave drag [Rind et al., 1988a] which can also drive the tropical upward mass flux. Inclusion of the gravity wave drag into the total wave activity for the correlation calculations (not shown) changes the peaks of correlation by about 10-20% but does not change the time lags discussed above.

## 4 Discussion and Conclusions

According to the downward control mechanism, the extratropical wave activity drives the tropical upward mass flux, which brings long-lived tracers with tropospheric sources into the stratosphere. The stratospheric tracer distribution is determined by a balance between transport and photochemical loss. For  $\text{N}_2\text{O}$ , the loss is dominant in the upper stratosphere, and its upper stratospheric mixing ratio lags the upper stratospheric wave activity by about 2 months. Strong wave episodes in winter induce peaks of mixing ratio in late winter to early spring. The interhemispheric asymmetry in wave activity is associated with a clear semiannual signal in the seasonal variation of the  $\text{N}_2\text{O}$  mixing ratio. For  $\text{CCl}_3\text{F}$ , the loss is dominant in the lower-middle stratosphere, where wave episodes are comparatively uniform in time although northern winter peaks are still evident. The resultant seasonal variation of the  $\text{CCl}_3\text{F}$  mixing ratio has an evident annual cycle but a vague semiannual signal.

QBO, which was not simulated in our models, modulates the tropical upward mass flux in the stratosphere and contributes the majority of the interannual variance in stratospheric tracer concentrations (e.g., upper stratospheric  $\text{CH}_4$  investigated in Randel et al. (1998)). Our model studies here cannot show the impacts of QBO on the interannual variation of the tracer budgets. However, the role of the model generated variation in planetary wave activity can then be studied without the modulation of QBO. Inclusion of QBO and the relative contributions of different natural forcings (e.g., QBO, ENSO, and aerosol effects) in driving the interannual variation in the tropical upward mass flux need further

studies by both model and observational data analyses.

In the literature, people working on CTMs usually recycle a 1-year wind archive until the models reach steady states. In this study, we see that the difference between these steady-state runs and runs using subsequent wind archives with interannual variation should be small. The wind archives generated by the GISS/GCMAM produce clear seasonal and interannual variations in both the  $\text{N}_2\text{O}$  and  $\text{CCl}_3\text{F}$  budgets (e.g., their stratospheric concentrations and loss rates). This illustrates how climate change (here we have the GCM generated wind variability) can affect long-lived tracer budgets through dynamical processes. The variation of the model tropical upward flux across 100 mb is consistent with the air mass flux variation obtained by the radiatively determined residual circulation [Rosenlof, 1995]. The magnitude of the CTM air mass flux in northern winter is smaller than the result in Rosenlof and Holton (1993), but that in southern winter is consistent with them.

Comparing the tropical upward tracer fluxes across 100 mb (not shown for  $\text{N}_2\text{O}$  and fig. 6b for  $\text{CCl}_3\text{F}$ ) with the total loss rates (fig. 5c and 6c for  $\text{N}_2\text{O}$  and  $\text{CCl}_3\text{F}$ , respectively), we find that about one-tenth of  $\text{N}_2\text{O}$  and one-third of  $\text{CCl}_3\text{F}$  entering the stratosphere from the tropical tropopause is dissociated in the stratosphere (the ratio is about the ratio of the lifetimes of the two tracers if the tropospheric mixing ratios are fixed as they are in our case). The remaining amount will be transported back to the troposphere in middle to high latitudes. The variation of the ventilation through tropical tropopause may affect the concentrations of other tracers in the upper troposphere, implying variations of the upper tropospheric chemistry in the tropics. Moreover, the variation of the mid-latitude downward flux across 100 mb implies variation of the extratropical stratosphere-troposphere exchange.

The annual mean lifetimes show the largest year-to-year variability of about 3-4% about the mean values of 121 yrs for  $\text{N}_2\text{O}$  and 31 yrs for  $\text{CCl}_3\text{F}$ , smaller than the seasonal variability which is over 10% about the mean values. Upper Atmospheric Research Satellite (UARS) may provide data necessary to verify the model variations in the stratospheric mixing ratios and the tracer lifetimes

[Minschwaner et al., 1998].

The theoretical framework by Plumb and Ko (1992) suggests a relation between the ratio of two tracers' lifetimes and the slope of the tracer-tracer correlation plot in the lower stratosphere,

$$\frac{\tau_1}{\tau_2} \simeq \frac{\psi_1}{\psi_2} \frac{d\psi_2}{d\psi_1} \quad (2)$$

where  $\tau$  is the tracer lifetime,  $\psi$  is the tracer mixing ratio, and  $\frac{d\psi_2}{d\psi_1}$  represents the slope of the tracer-tracer correlation plot. Scatter of data points is expected if both tracers undergo different chemistry in the stratosphere [Avallone and Prather, 1997; Hall and Prather, 1995]. Using equation (2), one can relate the interannual variability of tracer-tracer correlation to the interannual variability of tracer lifetimes, that is,

$$\Delta\left(\frac{d\psi_2}{d\psi_1}\right)/\left(\frac{d\psi_2}{d\psi_1}\right) \simeq \frac{\Delta\tau_1}{\tau_1} - \frac{\Delta\tau_2}{\tau_2} \quad (3)$$

where we have assumed the tropospheric mixing ratios do not have an interannual variation as they do in our simulations. From table 1 and equation (3), one can imply that the interannual variability of the  $\text{CCl}_3\text{F}$  and  $\text{N}_2\text{O}$  correlation plot is about 1-4%. Therefore, one cannot expect to detect it by looking at the model or observational tracer-tracer correlations because the signal is far smaller than the scatter of the plot [Avallone and Prather, 1997]. One can also infer that the variability of lifetimes discussed above has a very small effect on the estimates of several environmental indices which depend on the ratio of lifetimes of the tracers being concerned (e.g., Chlorine Loading Potential, etc).

**Acknowledgments.** We thank William J. Randel for providing the NMC data of E-P flux divergence, Steven Pawson for preparing the plots of figure 4, Patrick Lonergan for preparing the wind archives, Jean Lerner for providing graphic programs, and Tim Hall for invaluable discussions. We also thank the three anonymous reviewers for their invaluable comments to improve the manuscript. This work is supported by the NASA Atmospheric Chemistry and Modeling Program and the NASA Climate Program.

## References

- Avallone, L. M., and M. J. Prather: Tracer-tracer correlations: Three-dimensional model simulations and comparisons to observations. *J. Geophys. Res.*, 102, 19,233-19,246, 1997.
- Bowman, K. P. and A. J. Krueger: A global climatology of total ozone from Nimbus 7 total ozone mapping spectrometer. *J. Geophys. Res.*, 90, 7967-7976, 1985.
- Cunnold, D. M., R. F. Weiss, R. G. Prinn, D. Hartley, P. G. Simmonds, P. J. Fraser, B. Miller, F. N. Alyea, and L. Porter: GAGE/AGAGE measurements indicating reductions in global emissions of  $\text{CCl}_3\text{F}$  and  $\text{CCl}_2\text{F}_2$  in 1992-1994. *J. Geophys. Res.*, 102, 1259-1269, 1997.
- Hall, T. M., and R. A. Plumb: Age as a diagnostic of stratospheric transport. *J. Geophys. Res.*, 99, 1059-1070, 1994.
- Hall, T. M., and M. J. Prather: Simulations of the trend and annual cycle in stratospheric  $\text{CO}_2$ . *J. Geophys. Res.*, 98, 10,573-10,581, 1993.
- Hall, T. M., and M. J. Prather: Seasonal evolutions of  $\text{N}_2\text{O}$ ,  $\text{O}_3$ , and  $\text{CO}_2$ : Three-dimensional simulations of stratospheric correlations. *J. Geophys. Res.*, 100, 16,699-16,720, 1995.
- Haynes, P. H., C. J. Marks, M. E. McIntyre, T. G. Shepherd, and K. P. Shine: On the "downward control" of extratropical diabatic circulations by eddy-induced mean zonal forces. *J. Atmos. Sci.*, 48, 651-678, 1991.
- Holton, J. R.: Meridional distribution of stratospheric trace constituents. *J. Atmos. Sci.*, 43, 1238-1242, 1986.
- Holton, J. R., P. H. Haynes, M. E. McIntyre, A. R. Douglass, R. B. Rood, and L. Pfister: Stratosphere - Troposphere Exchange. *Rev. of Geophys.*, 33, 403-439, 1996.
- Ko, M. K. W., and C. H. Jackman: Model calculations of atmospheric lifetimes, chapter 5 in: *Report on concentrations, lifetimes and trends of CFCs, halons, and related species*, Kaye, J. A. et al. (eds.), NASA

- Office of Mission to Planet Earth, Science Division, Washington, D. C., USA, 5.1-5.33, 1994.
- Lou, G. P., F. N. Alyea, D. M. Cunnold, and T. P. Kindler: N<sub>2</sub>O transport in a three-dimensional model driven by U. K. Meteorological Office winds. *J. Geophys. Res.*, 102, 16,065-16,087, 1997.
- Mahlman, J., H. Levy, and W. Moxim: Three-dimensional simulations of stratospheric N<sub>2</sub>O: predictions for other trace constituents. *J. Geophys. Res.*, 91, 2687-2707, 1986.
- Minschwaner, K., R. W. Carver, B. P. Briegleb, and A. E. Roche: Infrared radiative forcing and atmospheric lifetimes of trace species based on observations from UARS. *J. Geophys. Res.*, 103, 23,243-23,253, 1998.
- Plumb, R. A., and M. K. W. Ko: Interrelationships between mixing ratios of long-lived stratospheric constituents. *J. Geophys. Res.*, 97, 10,145-10,156, 1992.
- Prather, M. J.: Numerical advection by conservation of second-order moments. *J. Geophys. Res.*, 91, 6671-6681, 1986.
- Prather, M. J.: The atmospheric effects of stratospheric aircraft: report of the 1992 models and measurements workshop. *NASA Ref. Pub. 1292*, 1, 76-89, 1993.
- Prather, M. J., R. Derwent, D. Ehhalt, P. Fraser, E. Sanhueza, and X. Zhou: Other trace gases and atmospheric chemistry, chapter 2 in: *Climate Change 1994, Radiative forcing of climate change and an evaluation of the IPCC IS92 emission scenarios*, Houghton, J. et al., (eds.), Interannual Pannel on Climate Change, Cambridge University Press, Cambridge, UK, 72-126, 1994.
- Prather, M. J., M. M. Garcia, R. Suozzo, D. Rind: Global impact of the antarctic ozone hole: Dynamical dilution with a three-dimensional chemical transport model. *J. Geophys. Res.*, 95, 3449-3471, 1990.

- Prather, M. J., and A. J. Jaffe: Global impact of the antarctic ozone hole: chemical propagation. *J. Geophys. Res.*, 95, 3473-3492, 1990.
- Prather, M. J., M. B. McElroy, S. C. Wofsy, G. Russell, and D. Rind: Chemistry of the global troposphere: Fluorocarbons as tracers of air motion. *J. Geophys. Res.*, 92, 6579-6613, 1987.
- Randel, W. J.: Global atmospheric circulation statistics, 1000-1 mb. NCAR technical note, TN-366+STR, 1992.
- Randel, W. J., B. A. Bovile, J. C. Gille, P. L. Bailey, S. T. Massie, J. B. Kumer, J. L. Mergenthaler, and A. E. Roche: Simulation of stratospheric N<sub>2</sub>O in the NCAR CCM2: Comparison with CLAES data and global budget analyses. *J. Atmos. Sci.*, 51, 2834-2845, 1994.
- Randel, W. J., F. Wu, J. M. Russell III, A. Roche, and J. W. Waters: Seasonal cycles and QBO variations in stratospheric CH<sub>4</sub> and H<sub>2</sub>O observed in UARS HALOE data. *J. Atmos. Sci.*, 55, 163-185, 1998.
- Rind, D., and N. K. Balachandran: Modeling the effects of UV variability and the QBO on the troposphere-stratosphere System. Part II: The troposphere. *J. Climate*, 8, 2080-2095, 1995.
- Rind, D., N. K. Balachandran, and R. Suozzo: Climate change and the middle atmosphere. Part II: The impact of volcanic aerosols. *J. Climate*, 5, 189-208, 1992.
- Rind, D., and P. Lonergan: Modeled impacts of stratospheric ozone and water vapor perturbations with implications for high-speed civil transport aircraft. *J. Geophys. Res.*, 100, 7381-7396, 1995.
- Rind, D., R. Suozzo, N. K. Balachandran, A. Lacis and G. Russell: The GISS global climate-middle atmosphere model. Part I: Model structure and climatology. *J. Atmos. Sci.*, 45, 329-367, 1988a.
- Rind, D., R. Suozzo, N. K. Balachandran, A. Lacis and G. Russell: The GISS global climate-middle atmosphere model. Part II: Model variability due to interactions between planetary waves, the mean circulation

- and gravity wave drag. *J. Atmos. Sci.*, 45, 371-386, 1988b.
- Rind, D., R. Suozzo, N. K. Balachandran, M. J. Prather: Climate change and the middle atmosphere. Part I: The doubled CO<sub>2</sub> climate. *J. Atmos. Sci.*, 47, 475-494, 1990.
- Rosenlof, K. H.: Seasonal cycle of the residual mean meridional circulation in the stratosphere. *J. Geophys. Res.*, 100, 5173-5191, 1995.
- Rosenlof, K. H., and J. R. Holton: Estimates of the stratospheric residual circulation using the downward control principles, *J. Geophys. Res.*, 98, 10,465-10,479, 1993.
- Shindell, D. T., S. Wong, D. H. Rind: The interannual variability of the Antarctic Ozone Hole in a GCM. Part I: The influence of tropospheric wave variability. *J. Atmos. Sci.*, 54, 2308-2317, 1997.
- Strahan, S. E., J. E. Nielsen and M. C. Cerniglia: Long-lived tracer transport in the Antarctic stratosphere. *J. Geophys. Res.*, 101, 26,615-26,629, 1996.
- Ushimaru, S. and H. Tanaka: The role of planetary waves in the formation of inter-hemispheric asymmetry in ozone distribution. *J. of Meteor. Soc. of Japan*, 72, 653-670, 1994.
- Volk, C. M., J. W. Elkins, D. W. Fahey, G. S. Dutton, J. M. Gilligan, M. Loewenstein, J. R. Podolske, K. R. Chan, and M. R. Gunson: Evaluation of source gas lifetimes from stratospheric observations. *J. Geophys. Res.*, 102, 25,543-25,564, 1997.
- Yulaeva, E., J.R. Holton, and J. M. Wallace: On the cause of the annual cycle in tropical lower stratospheric temperatures. *J. Atmos. Sci.*, 51, 169-174, 1994.

Figure 1. Evolution of the  $\text{N}_2\text{O}$  distribution and flux. (a) The zonal mean  $\text{N}_2\text{O}$  mixing ratio (in ppbv) averaged from 10 mb to 1 mb; (b) the zonal mean  $\text{N}_2\text{O}$  flux (in  $10^{-12}$  kg/m<sup>2</sup>/s) across 10 mb. The x-axis is for simulation year and the y-axis is for latitude.

Figure 2. Evolution of the  $\text{CCl}_3\text{F}$  distribution and flux. (a) The zonal mean  $\text{CCl}_3\text{F}$  mixing ratio (in pptv) averaged from 100 mb to 10 mb; (b) the zonal mean  $\text{CCl}_3\text{F}$  flux (in  $10^{-13}$  kg/m<sup>2</sup>/s) across 100 mb. The x-axis is for simulation year and the y-axis is for latitude.

Figure 3. Evolution of the model stratospheric planetary wave activity, represented by the E-P flux convergence (in m/s/day), (a) averaged from 10 mb to 1 mb; (b) averaged from 100 mb to 5 mb. The x-axis is for simulation year and the y-axis is for latitude.

Figure 4. Evolution of the NMC stratospheric planetary wave activity, represented by the E-P flux divergence (in m/s/day), averaged from 10 mb to 1 mb (top panel, contour interval 2.5), and from 100 mb to 5 mb (bottom panel, contour interval 0.5) [Randel, 1992].

Figure 5. Time series of several averaged variables for  $\text{N}_2\text{O}$ . (a) The E-P flux convergence (in m/s/day) averaged from 8° to 40° in latitude and from 10 mb to 1 mb in altitude, with the dotted line representing the northern hemisphere, the dashed line the southern hemisphere, and the solid line the sum of values from both hemispheres; (b) the tropical upward  $\text{N}_2\text{O}$  flux (in  $10^{-12}$  kg/m<sup>2</sup>/s) across 10 mb, averaged from 24°S to 24°N in latitude; (c) the global  $\text{N}_2\text{O}$  loss rate (in  $10^{-12}$  kg/m<sup>2</sup>/s); (d) the zonal mean  $\text{N}_2\text{O}$  mixing ratio (in ppbv) averaged from 30°S to 30°N in latitude and from 10 mb to 1 mb in altitude.

Figure 6. Time series of several averaged variables for  $\text{CCl}_3\text{F}$ . (a) The E-P flux convergence (in  $\text{m/s/day}$ ) averaged from  $8^\circ$  to  $72^\circ$  in latitude and from 100 mb to 5 mb in altitude, with the dotted line representing the northern hemisphere, the dashed line the southern hemisphere, and the solid line the sum of values from both hemispheres; (b) the tropical upward  $\text{CCl}_3\text{F}$  flux (in  $10^{-14} \text{ kg/m}^2/\text{s}$ ) across 100 mb, averaged from  $30^\circ\text{S}$  to  $30^\circ\text{N}$ ; (c) the global  $\text{CCl}_3\text{F}$  loss rate (in  $10^{-14} \text{ kg/m}^2/\text{s}$ ); (d) the zonal mean  $\text{CCl}_3\text{F}$  mixing ratio (in pptv) averaged from  $55^\circ\text{S}$  to  $55^\circ\text{N}$  in latitude and from 100 mb to 10 mb in altitude.

Figure 7. Time-lag correlations for (a) the adjacent  $\text{N}_2\text{O}$  time series from Figure 4; (b) the adjacent  $\text{CCl}_3\text{F}$  time series from Figure 5. Dotted lines represent correlations between the extratropical wave activity and the upward flux, dashed lines, between the upward flux and the global loss rate, dash-dot lines, between the global loss rate and the averaged mixing ratio, and solid lines, between the wave activity and the averaged mixing ratio.

Table 1. The seasonal and interannual variability in the N<sub>2</sub>O and CCl<sub>3</sub>F lifetimes (in yrs).

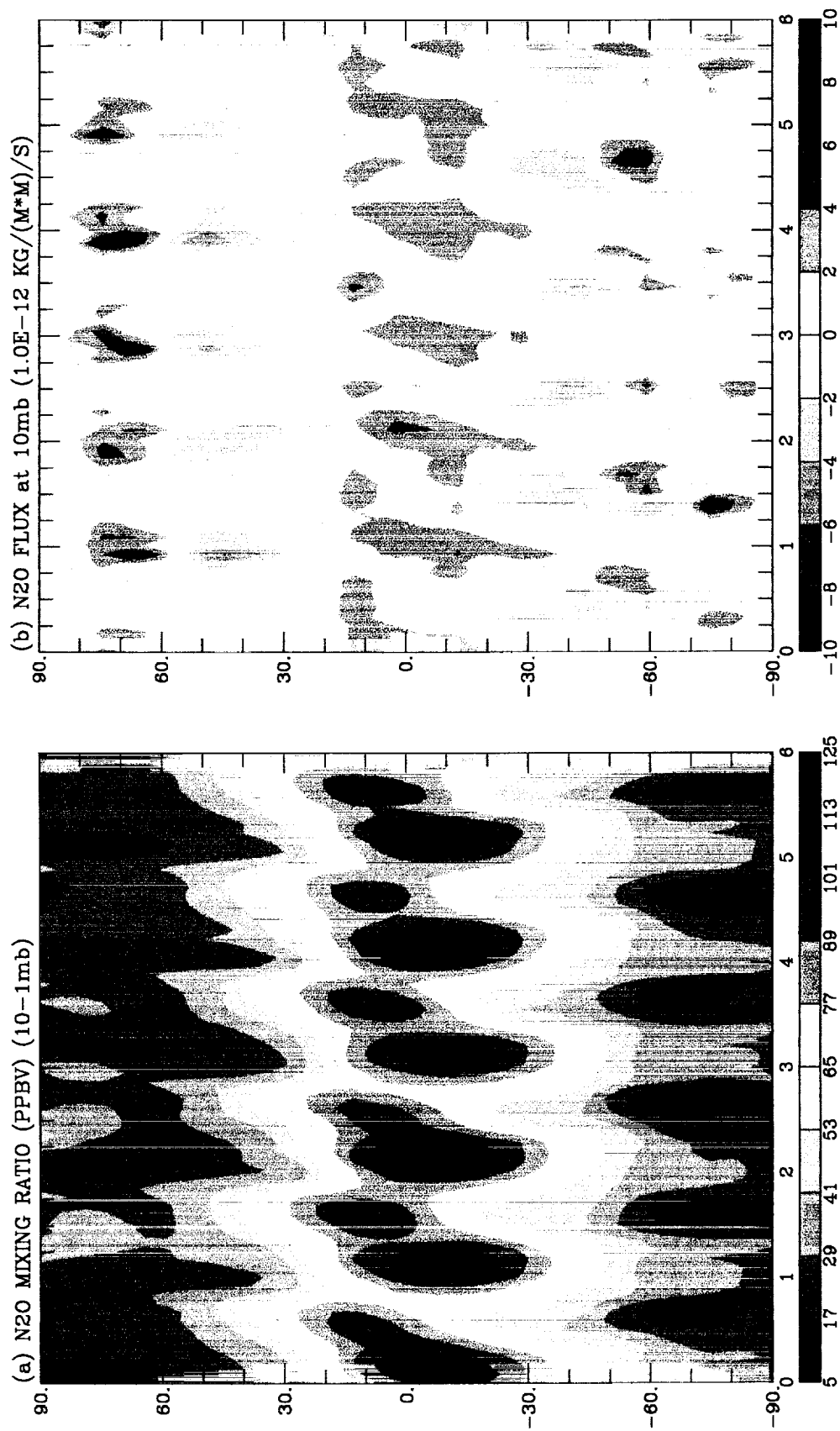
	JAN	APR	JUL	OCT	Annual mean
N <sub>2</sub> O					
1.	109.3	118.4	130.2	129.8	122.2
2.	109.8	120.5	125.5	124.8	120.2
3.	109.6	118.6	129.7	129.8	121.1
4.	108.5	125.1	129.7	128.4	123.2
5.	107.2	115.7	129.6	125.4	119.9
6.	110.7	119.0	126.3	123.6	120.5
Average	109.2	119.6	128.5	127.0	121.2
Max. Changes (%)	3.2	7.9	3.7	3.9	2.7
CCl <sub>3</sub> F					
1.	30.3	30.1	34.1	31.2	31.5
2.	29.8	29.7	33.2	30.0	30.6
3.	29.9	30.5	34.0	31.4	31.3
4.	30.2	31.3	34.3	31.1	31.8
5.	29.7	30.3	34.2	30.7	31.5
6.	31.1	31.1	33.6	29.0	31.1
Average	30.2	30.5	33.9	30.6	31.3
Max. Changes (%)	4.6	5.2	3.2	7.8	3.8

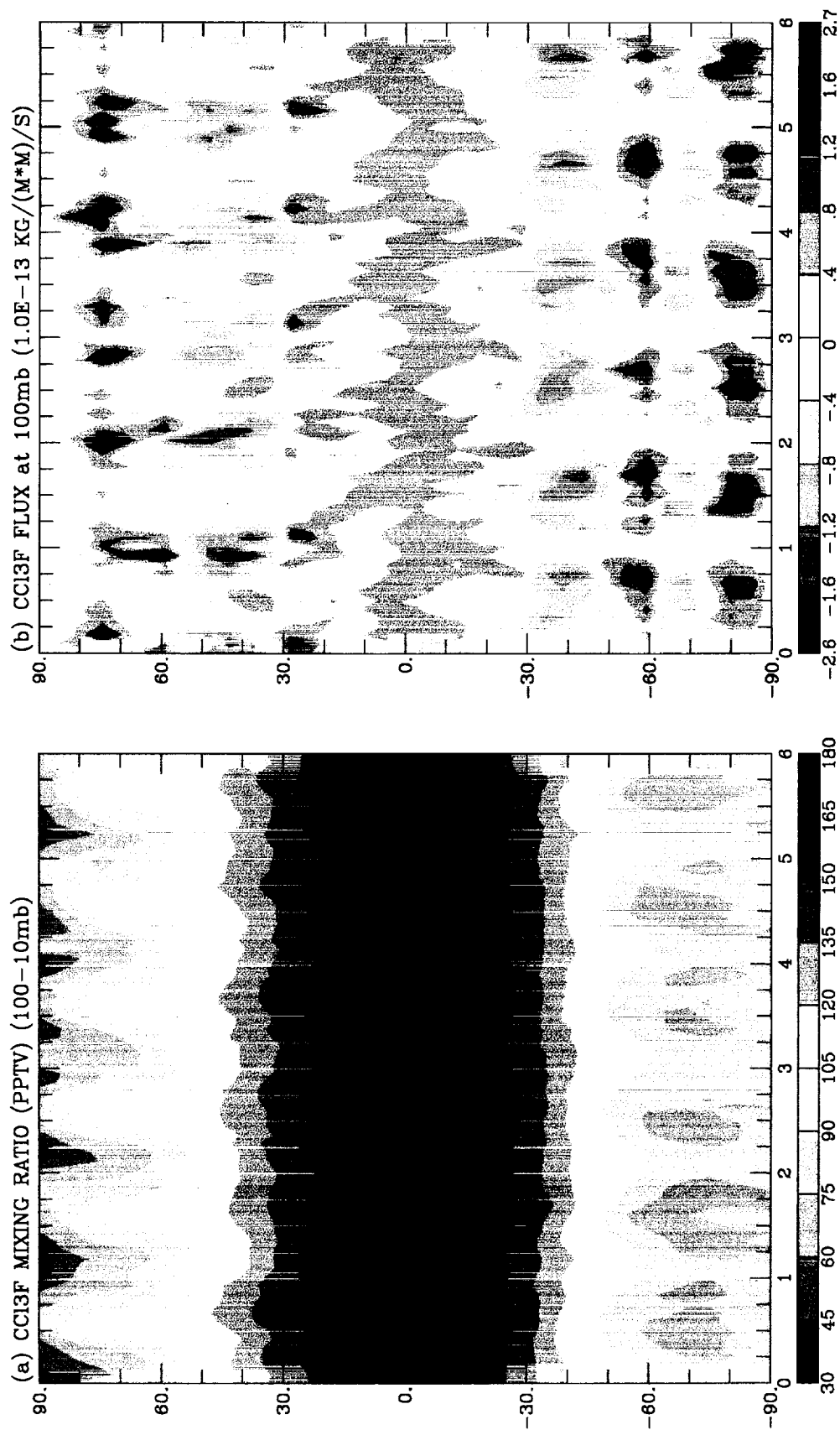
Note: In last column are the annual mean lifetimes, and in the last row of each section are the largest peak-to-peak interannual differences in the corresponding columns (in percentage about the corresponding column mean values).

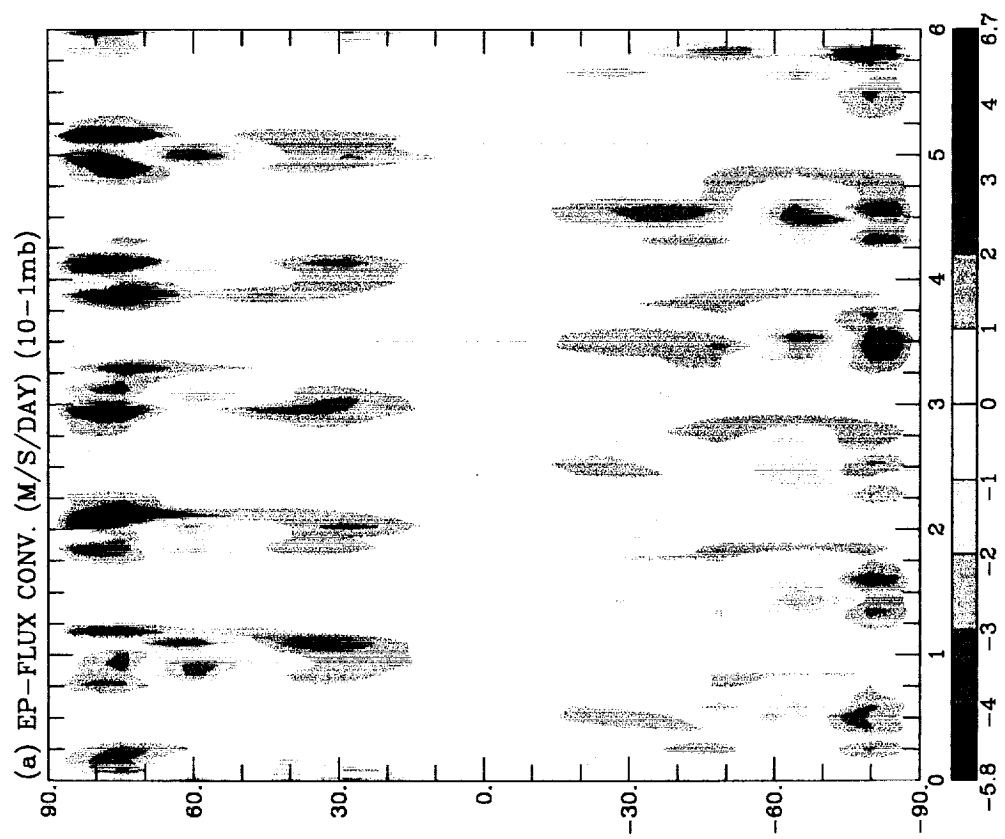
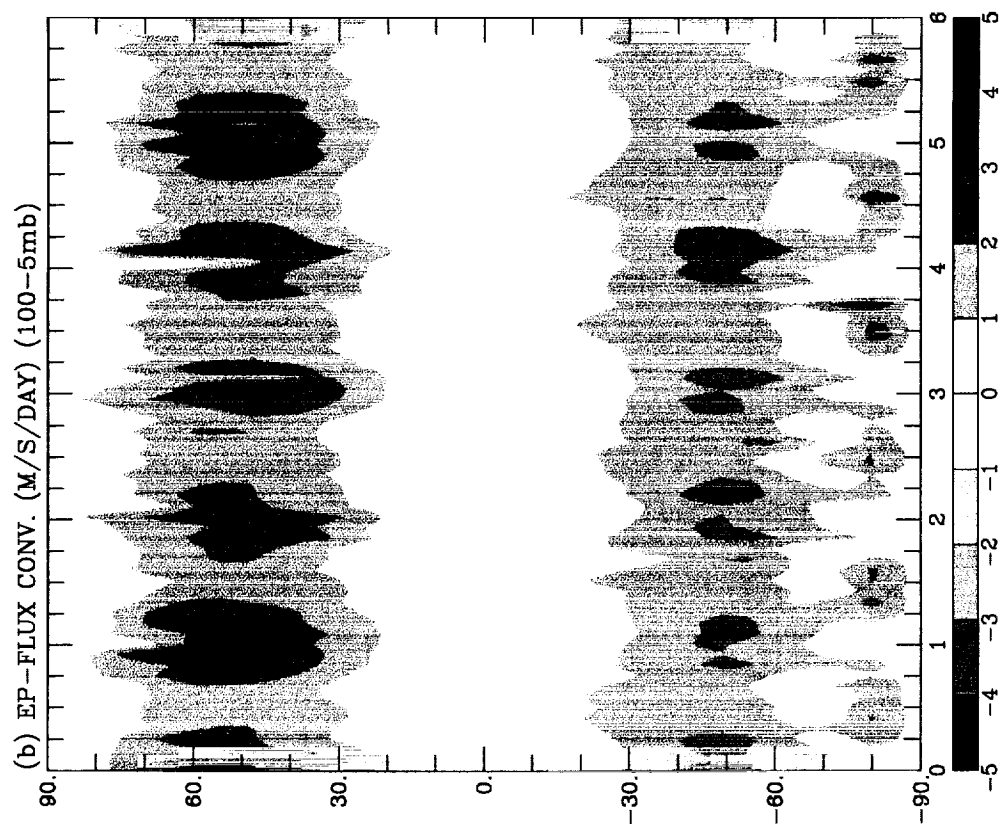
Table 2. Comparison of the tropical upward mass flux (in  $10^8$  kg/s).

Data Source	DJF	JJA	Annual mean
Rosenlof and Holton (1993)	114	56	85
Rosenlof (1995) (at 70 mb)	66.4	43.2	54.8
Our CTM	88	50	69

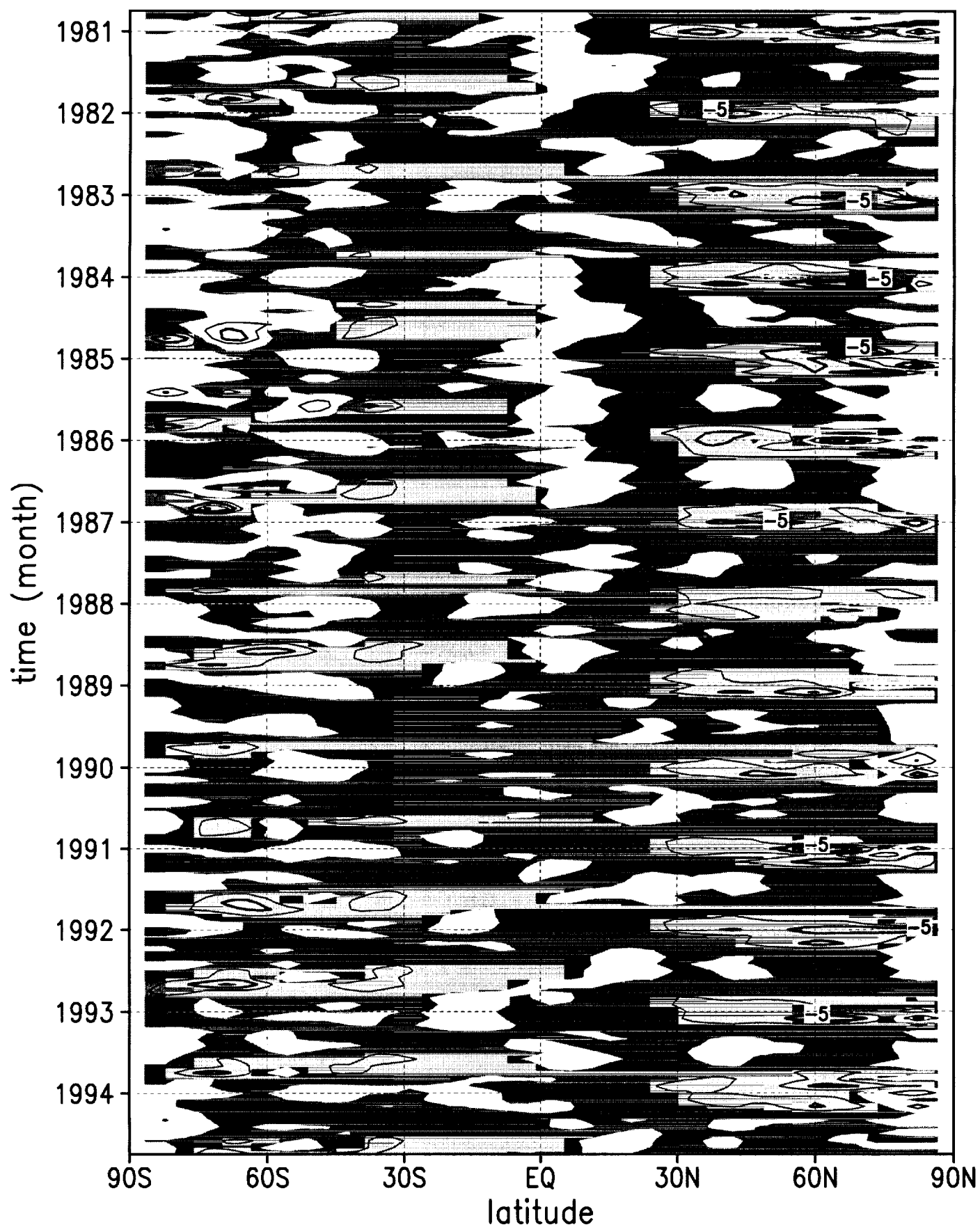
Note: The data of Rosenlof (1995) are presented at 70 mb and for January and July only, instead of for the DJF and JJA seasons. The last column is simply the average of the DJF and JJA column data.



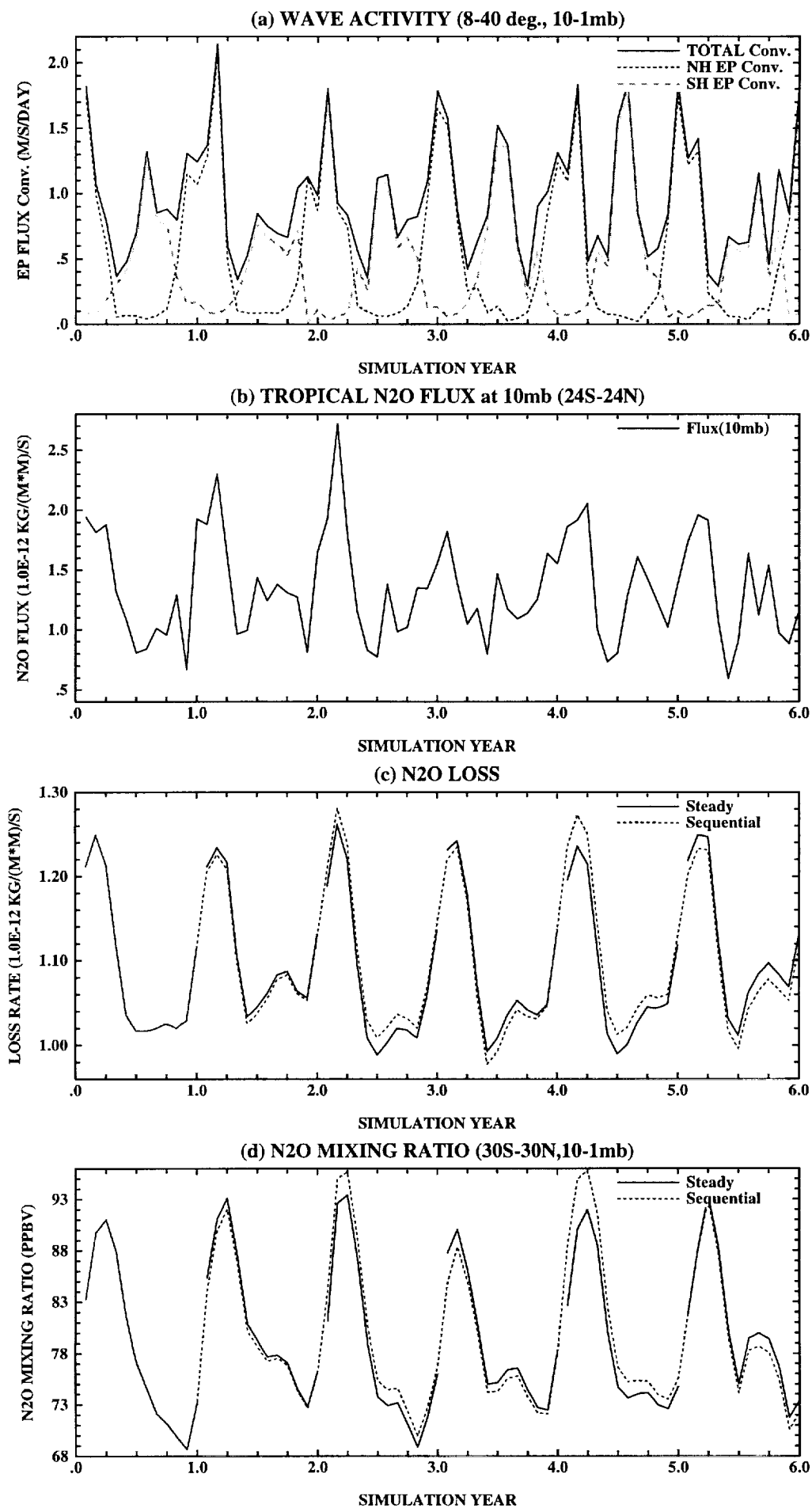


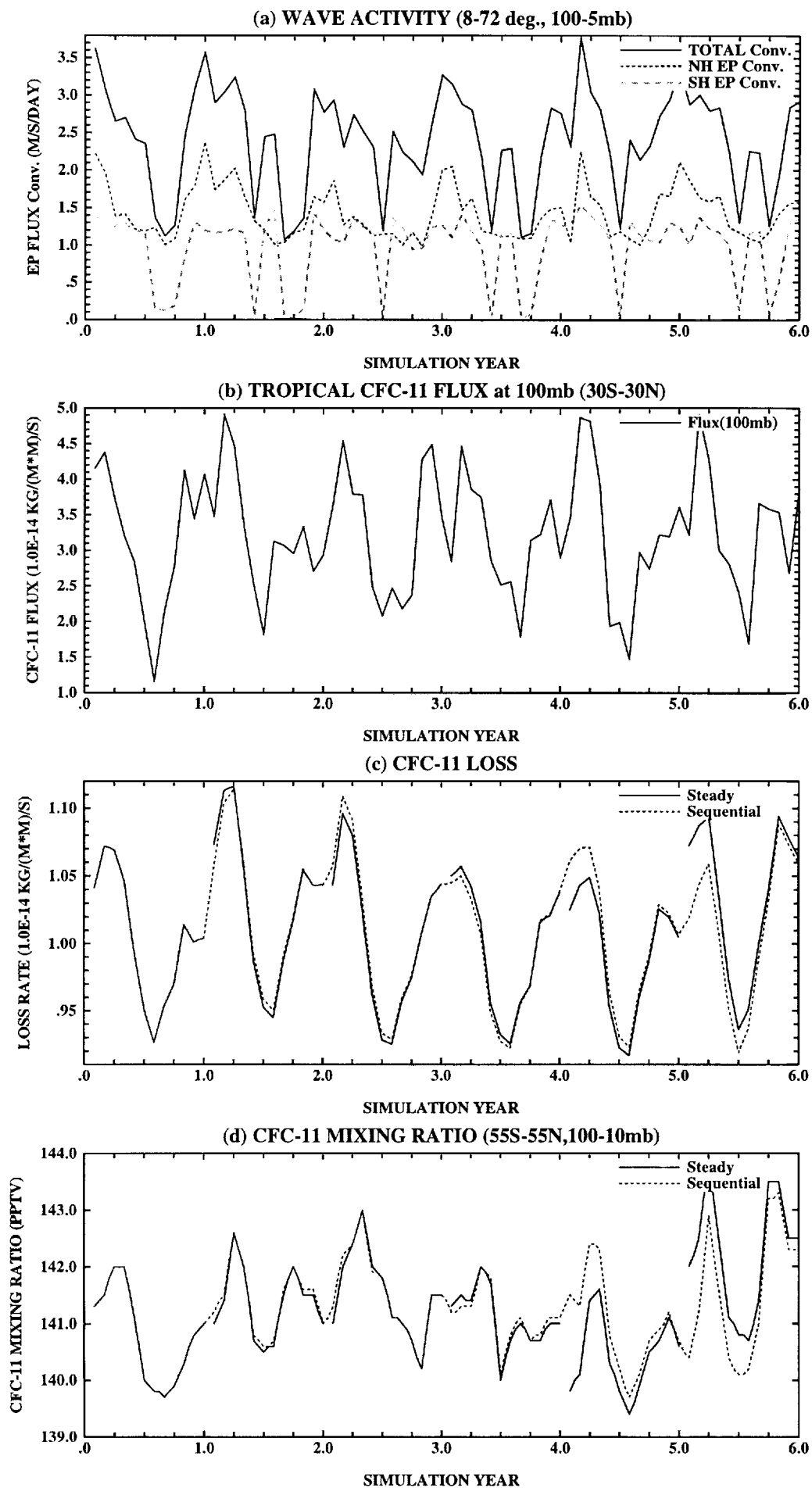


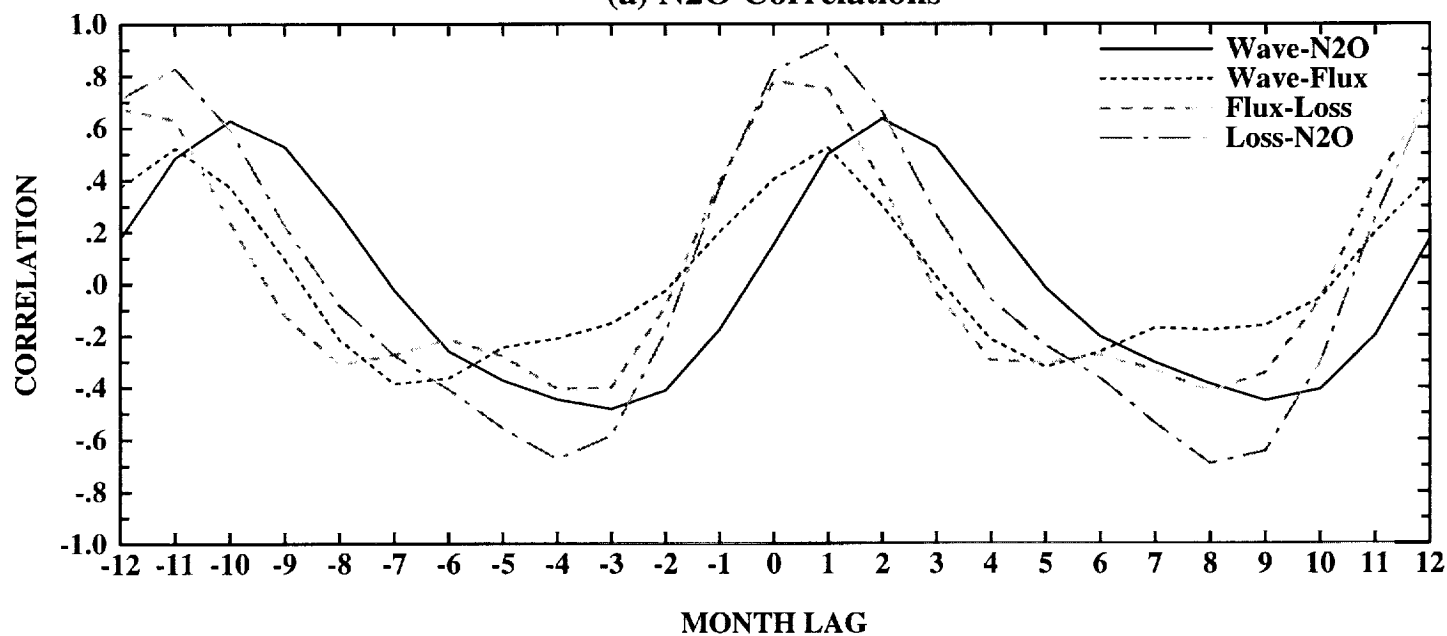
## E-P Flux Div. (m/s/day): 10–1Pa









(a) N<sub>2</sub>O Correlations(b) CCl<sub>3</sub>F Correlations